Evaluating arbitrary strain configurations and doping in graphene with Raman spectroscopy

2D Materials

OPEN ACCESS

RECEIVED
10 July 2017

REVISED
8 September 2017

ACCEPTED FOR PUBLICATION
3 October 2017

PUBLISHED
6 November 2017

PAPER

Evaluating arbitrary strain configurations and doping in graphene with Raman spectroscopy

Niclas S Mueller[1], Sebastian Heeg[2,3], Miriam Peña Alvarez[4], Patryk Kusch[1], Sören Wasserroth[1], Nick Clark[2], Fredrik Schedin[8], John Parthenios[5], Konstantinos Papagelis[5,6], Costas Galiotis[5,7], Martin Kalbáč[4], Aravind Vijayaraghavan[2,8], Uwe Huebner[9], Roman Gorbachev[10], Otakar Frank[4] and Stephanie Reich[1]

[1] Department of Physics, Freie Universität Berlin, Arnimallee 14, D-14195 Berlin, Germany
[2] School of Materials, The University of Manchester, Manchester M13 9PL, United Kingdom
[3] Photonics Laboratory, ETH Zürich, 8093 Zürich, Switzerland
[4] J Heyrovský Institute of Physical Chemistry, Academy of Sciences of the Czech Republic, Dolejškova 3, CZ-18223 Prague 8, Czechia
[5] Institute of Chemical Engineering Sciences, Foundation of Research and Technology—Hellas, Patras 26504, Greece
[6] Department of Physics, University of Patras, Patras 26504, Greece
[7] Department of Chemical Engineering, University of Patras, Patras 26504, Greece
[8] National Graphene Institute, University of Manchester, Manchester M13 9PL, United Kingdom
[9] Leibnitz Institute of Photonic Technology, 07745 Jena, Germany
[10] School of Physics & Astronomy, The University of Manchester, Manchester M13 9PL, United Kingdom

E-mail: niclasm@physik.fu-berlin.de **and** reich@physik.fu-berlin.de

Keywords: graphene, Raman, strain, doping, correlation analysis, circular polarization

Supplementary material for this article is available online

Abstract

The properties of graphene depend sensitively on strain and doping affecting its behavior in devices and allowing an advanced tailoring of this material. A knowledge of the strain configuration, i.e. the relative magnitude of the components of the strain tensor, is particularly crucial, because it governs effects like band-gap opening, pseudo-magnetic fields, and induced superconductivity. It also enters critically in the analysis of the doping level. We propose a method for evaluating unknown strain configurations and simultaneous doping in graphene using Raman spectroscopy. In our analysis we first extract the bare peak shift of the G and 2D modes by eliminating their splitting due to shear strain. The shifts from hydrostatic strain and doping are separated by a correlation analysis of the 2D and G frequencies, where we find $\Delta\omega_{2D}/\Delta\omega_G = 2.21 \pm 0.05$ for pure hydrostatic strain. We obtain the local hydrostatic strain, shear strain and doping without any assumption on the strain configuration prior to the analysis, as we demonstrate for two model cases: Graphene under uniaxial stress and graphene suspended on nanostructures that induce strain. Raman scattering with circular corotating polarization is ideal for analyzing frequency shifts, especially for weak strain when the peak splitting by shear strain cannot be resolved.

Being the first two-dimensional material discovered, graphene has attracted a lot of attention for its extraordinary properties [1]. Ultra-high carrier mobility, large thermal and electrical conductivity, impermeability to any gases and extreme mechanical robustness are combined in one material [2]. Two-dimensional materials like graphene are strongly affected by their environment and distortions introduced during their processing. Locally varying strain is induced in the graphene lattice upon deposition on a substrate [3–5], thermal annealing [6] and stacking with other 2D materials [7, 8]. The substrate and adsorbed or intercalated substances typically induce a Fermi level shift and dope graphene [9, 10]. Strain and charge transfer doping both affect the electronic, chemical and optical properties of graphene, which ultimately determines its performance in devices. On the other hand, strain can be intentionally induced to engineer the properties of graphene giving rise to a new field called 'straintronics' [11]. Biaxial strain and doping greatly enhance electron–phonon coupling and potentially turn graphene into a superconductor, whereas non-uniform strain may induce pseudo-magnetic fields as high as 300 T and open a band gap in the electronic band structure [12–14].

Raman spectroscopy emerged as a powerful and non-destructive tool for characterizing the local properties of graphene [15, 16]. Doping and hydrostatic strain both lead to a shift of the Raman modes and shear strain to a peak splitting [17–19]. Lee *et al* suggested to separate the contributions of strain and doping with a correlation analysis of the G and 2D frequencies [20]. This approach has been extensively used for accessing the local properties of graphene on various substrates [5, 7, 21–27]. A serious drawback of the approach is that the strain configuration has to be known prior to the analysis. Moreover, strain is not exclusively either uniaxial or biaxial in character. A mixture between these two strain configurations cannot be treated within the correlation analysis [20]. The resulting uncertainties in the magnitude of strain and doping may exceed an order of magnitude. Furthermore, the strain configuration crucially determines the properties of graphene, such as band-gap opening, pseudo-magnetic fields and lifting of degeneracies [13, 14]. It is highly desirable to develop an analysis based on Raman spectroscopy that reliably determines the magnitude and configuration of the strain state plus doping.

Here, we show how to extract the magnitudes of hydrostatic strain, shear strain and doping from the Raman spectra for any (unknown) strain configuration and simultaneous doping. The peak splitting from shear strain is removed from the spectra by calculating the mean frequencies of the G^- and G^+ as well as the $2D^-$ and $2D^+$ modes. Hydrostatic strain and doping are determined with a correlation analysis of the G and 2D mean frequencies. The shear strain is obtained from the G peak splitting. We demonstrate two experimental approaches that can be used to conduct this strain-doping analysis. Recording Raman spectra with circularly polarized light is ideal for extracting the hydrostatic strain component at small strain where no peak splitting is visible as we show for graphene under uniaxial stress. We then apply our strain analysis to a complex case of graphene covering nanostructures for which the strain configuration is unknown. Graphene is suspended on lithographically fabricated gold nanodiscs forming dimers, which induce strong local and non-uniform strain in the graphene bridging the gap between the two nanoparticles. Surface-enhanced Raman scattering probes the local strain and doping levels on the nanoscale. The two examples serve as model cases for unraveling the strain and doping levels of graphene on arbitrary substrates.

1. Results and discussion

1.1. Methodology

Before introducing our method for strain-doping evaluation, we discuss the approach suggested by Lee *et al* [20] which has been used in many studies [5, 7, 21–27]. A sketch of the correlation analysis is shown in figure 1(a). The frequencies expected for purely strained and purely doped graphene are plotted as lines resembling a coordinate system in the $\omega_{2D} - \omega_G$ plot. Extracting strain and doping for a potential frequency pair $\{\omega_G, \omega_{2D}\}_{exp}$ is done by projecting the point onto the strain and doping axes. One thereby obtains the frequency shifts induced by doping and strain from which one can calculate the magnitude of strain and doping using reference values. The slope $\Delta\omega_{2D}/\Delta\omega_G$ for pure doping is <1 because the G frequency depends much stronger on doping than the 2D frequency [17, 28–30]. This is mostly attributed to a nonadiabatic Kohn anomaly at the Γ point in the phonon dispersion relation [31, 32]. Strain leads to a slope of ∼2 since the 2D mode is a phonon overtone that shifts with approximately twice the rate of a single phonon excitation (G line).

The value of the strain-related slope depends sensitively on the strain configuration[18, 33–38]. This leads to large uncertainties when separating the frequency shifts from strain and doping, as is schematically illustrated for an ω_{2D}, ω_G pair in figure 1(a). Bronsgeest *et al* noticed the ambiguity when analyzing the Raman spectra of graphene on cobalt [26]. They demonstrated that their strain was determined as 0.4% assuming a biaxial strain configuration, but more than twice as large (1%) for uniaxial strain. The uncertainty in the magnitude of the strain carries over to the charge density of the doping. For example, we obtain a frequency pair of $\omega_G = 1579\ cm^{-1}$, $\omega_{2D} = 2619\ cm^{-1}$ from figure 2(b), ↕↕. Assuming biaxial strain as the underlying configuration we find a charge density of $p = 3 \cdot 10^{13}\ cm^{-2}$, see below for details. Assuming uniaxial strain, on the other hand, $\Delta\omega_{2D}/\Delta\omega_G$ varies between 0.8 and 5.3 depending on which peak components were measured and in which crystallographic direction the strain was applied [33]. The corresponding *p*-type doping ranges from $5 \cdot 10^{12}\ cm^{-2}$ to $> 10^{14}\ cm^{-2}$ [17]. As we will show below, the graphene giving rise to the spectrum in figure 2(b), ↕↕ is uniaxially strained and p doped with a charge density of $5 \cdot 10^{12}\ cm^{-2}$. The correct value is obtained by a strain slope of 5.3.

To overcome these ambiguities, we suggest decomposing the effect of strain on the Raman spectrum into its fundamental components, i.e. the frequency shift and the frequency splitting, prior to the correlation analysis. Let us consider a general, unknown strain tensor

$$\varepsilon(\mathbf{r}) = \begin{pmatrix} \varepsilon_{xx}(\mathbf{r}) & \varepsilon_{xy}(\mathbf{r}) \\ \varepsilon_{yx}(\mathbf{r}) & \varepsilon_{yy}(\mathbf{r}) \end{pmatrix}, \quad (1)$$

with in-plane components ε_{ij}. By solving the secular equation, we calculate the phonon shift rates as [18, 19, 39, 40]

$$\Delta\omega_{pn}^{\pm} = -\omega_{pn}^0\gamma_{pn}\left(\varepsilon_{xx}+\varepsilon_{yy}\right) \pm \frac{1}{2}\omega_{pn}^0\beta_{pn}\sqrt{\left(\varepsilon_{xx}-\varepsilon_{yy}\right)^2+4\varepsilon_{xy}^2}, \quad (2)$$

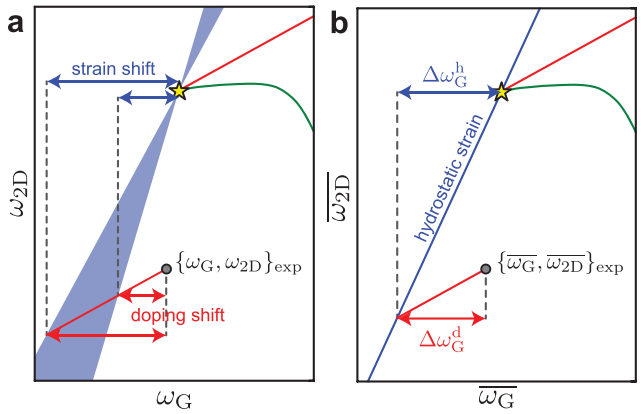

Figure 1. Correlation analysis of 2D and G frequencies to separate the frequency shifts from strain and doping. The expected frequencies are illustrated by a yellow star for no strain and no doping, a blue area/line for strain, a red line for *p*-type doping and a green line for *n*-type doping. (a) Correlation analysis suggested in [20]. Reference values for the strain shift rates deviate from each other and depend on the underlying strain configuration. The frequency shifts from strain and doping cannot be separated for a potential data point $\{\omega_G, \omega_{2D}\}_{exp}$ (shown for p doping). (b) Correlation analysis based on the mean frequencies $\overline{\omega_G}$ and $\overline{\omega_{2D}}$ (see equation (3)). The frequency shifts expected for pure hydrostatic strain can be used as reference values for any strain configuration. The separation of G frequency shifts from doping $\Delta\omega_G^d$ and strain $\Delta\omega_G^h$ is exemplarily shown for the case of p doping.

with the phonon frequency in the absence of strain ω_{pn}^0, the Grueneisen parameter γ_{pn} and the shear-strain phonon deformation potential β_{pn}. Any strain configuration can be decomposed into a hydrostatic component $\varepsilon_h = \varepsilon_{xx} + \varepsilon_{yy}$ and a shear component $\varepsilon_s = \sqrt{(\varepsilon_{xx} - \varepsilon_{yy})^2 + 4\varepsilon_{xy}^2}$ (assuming $\varepsilon_{xy} = \varepsilon_{yx}$) [40]. Hydrostatic strain corresponds to an isotropic increase or decrease in the size of the graphene lattice; it leads to a frequency shift $\Delta\omega_{pn}^h = -\omega_{pn}^0 \gamma_{pn} \varepsilon_h$ determined by the Grueneisen parameter γ_{pn} [37]. Note that from its definition $\varepsilon_h = \varepsilon_{xx} + \varepsilon_{yy}$ the hydrostatic strain is twice as large as the corresponding biaxial strain $\varepsilon_b = \varepsilon_{xx} = \varepsilon_{yy}$. Shear strain corresponds to an anisotropic distortion of the graphene lattice leaving the area of the unit cell unchanged. It leads to a peak splitting $\Delta\omega_{pn}^s = \omega_{pn}^0 \beta_{pn} \varepsilon_s$ that depends on the shear deformation potential β_{pn}, while the mean position of the two peak components remains constant [18, 41]. Equation (2) is strictly valid for first-order Raman processes such as the G mode. For higher-order processes like the 2D mode, the electronic structure and its dependence on strain have to be considered as well. The general concept of peak splitting by shear strain and peak shift by hydrostatic strain, however, also applies to the 2D mode, as was shown experimentally and theoretically [33, 37, 42–44]. In the following, the peak components are labeled G^- and G^+ for the G mode and $2D^-$ and $2D^+$ for the 2D mode.

We propose an evaluation of arbitrary strain configurations and simultaneous doping in graphene that is based on the phonon frequency shift induced by the hydrostatic strain component:

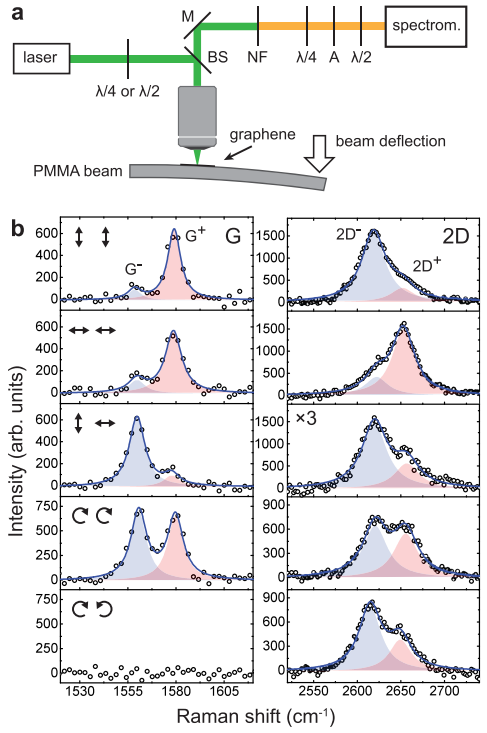

Figure 2. Polarized Raman spectroscopy of uniaxially-strained graphene. (a) Backscattering Raman setup with control of light polarization ($\lambda/4$—quarter-wave plate, $\lambda/2$—half-wave plate, BS—beam splitter, M—mirror, NF—notch filter, A—analyzer). For circular light polarization, two $\lambda/4$ plates, an analyzer and one $\lambda/2$ plate are used. (b) Raman spectra of the G and 2D mode of uniaxially-strained graphene (laser wavelength 532 nm). Fits with two Lorentzian peaks are superimposed on the experimental data. G^- and $2D^-$ peaks are colored blue, G^+ and $2D^+$ peaks are colored red. Polarizations of the incoming- and outgoing light are indicated by arrows (↕—linear along strain, ↔—linear perpendicular to strain, ↻↻—circular corotating, ↻↺—circular contrarotating).

1. To obtain the frequency shift by hydrostatic strain, we eliminate the peak splitting from shear strain $\Delta\omega_s$ by considering the mean frequencies

$$\overline{\omega_G} = \frac{\omega_{G^-} + \omega_{G^+}}{2}, \quad \overline{\omega_{2D}} = \frac{\omega_{2D^-} + \omega_{2D^+}}{2}. \quad (3)$$

   This leads to a data point in the correlation plot that is only affected by hydrostatic strain and doping (see figure 1(b)).
2. The peak shifts from hydrostatic strain $\Delta\omega^h_{pn}$ and doping $\Delta\omega^d_{pn}$ are separated with a correlation analysis of $\overline{\omega_G}$ and $\overline{\omega_{2D}}$, following [20]. The slope expected for hydrostatic strain is used as a reference (illustrated in figure 1(b)).
3. Hydrostatic strain ε_h is calculated from the G mode shift $\Delta\omega^h_G$ and doping from $\Delta\omega^d_G$.
4. Shear strain ε_s is calculated from the G splitting $\Delta\omega^s_G$.

The approach requires no knowledge of the strain configuration as an input parameter. The type of doping needs to be known for choosing the correct reference values. For many graphene-material combinations it is available in the literature; alternatively it may be obtained from reference measurements with other techniques.

1.2. Analysis with circular light polarization

In the following, we present two examples for how to apply our methodology. These can be viewed as model cases for the strain analysis of graphene on arbitrary substrates. As a first example, we show that circular light polarization is ideal for measuring the mean frequencies $\overline{\omega_G}$ and $\overline{\omega_{2D}}$. We use a Raman setup where linear and circular light polarization can be independently chosen for incoming and scattered light (figure 2(a), see methods for details). Tensile uniaxial strain is induced in exfoliated monolayer graphene flakes by the deflection of a poly(methyl methacrylate) (PMMA) beam (figure 2(a)) [18, 45–48]. We observe a shift of the phonon frequencies to lower wavenumber because of hydrostatic strain and a peak splitting because of shear strain (figure 2(b)). For linearly polarized incoming and scattered light, the +/− components differ strongly in intensity for different polarization configurations (figure 2(b), ↕↕, ↔↔ and ↕↔). From the intensity ratio of G^- and G^+ peak, we find that the uniaxial strain direction is primarily along the zigzag direction with a misorientation of 7.5% (see methods, equation (4)) [18, 19].

The G^- and G^+ peak are of equal intensity for circular corotating polarization as expected from the selection rules (figure 2(b), ↻↻, see methods for discussion). A similar behavior was observed for the 2D mode. Both G^- and G^+ modes vanished for circular contrarotating polarization (figure 2(b), ↻↺). For this polarization, the 2D mode split into components of unequal intensity; the $2D^-$ component was consistently more intense than the $2D^+$ component. A similar behavior was visible for strain along the armchair direction in the graphene lattice (supplementary figure S1 (stacks.iop.org/2DM/5/015016/mmedia)).

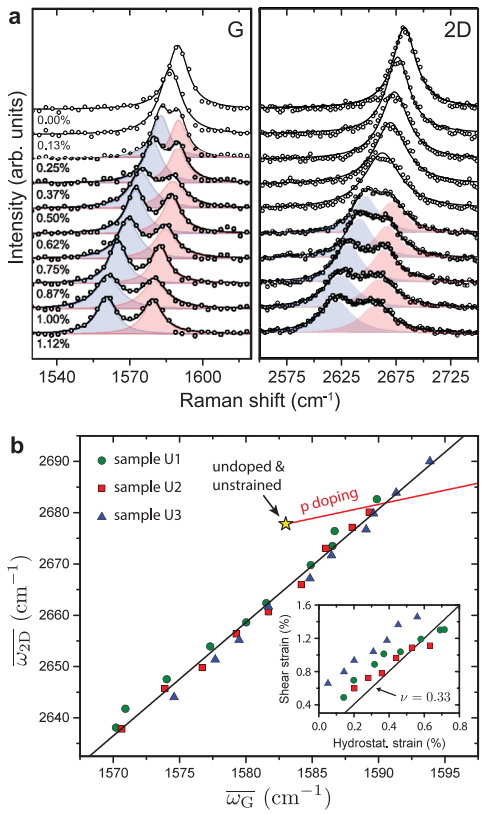

Figure 3. Extracting the hydrostatic strain, shear strain and doping from the Raman spectra of uniaxially-strained graphene using circular corotating polarization (laser wavelength 532 nm). (a) G and 2D mode of graphene under uniaxial strain which increases incrementally from top to bottom (sample U1). Fits with one or two Lorentzian peaks are superimposed on the data. G^- and $2D^-$ peaks are colored blue, G^+ and $2D^+$ peaks are colored red. Plots are labeled by the expected uniaxial strain $\varepsilon_u = \varepsilon_h/(1-\nu) = \varepsilon_s/(1+\nu)$ calculated from the beam deflection [45]. (b) Correlation plot of 2D and G mean frequencies for three samples (U1–U3). A linear fit is plotted as a solid line. The red line indicates the expected spectral positions if only *p*-type doping is present (slope of 0.55, see [30]). The yellow star indicates the spectral position in the absence of doping and strain (extracted from [17], 514 nm laser excitation, assuming a 2D mode dispersion of 100 cm^{-1} eV^{-1}). The inset shows the shear strain as a function of hydrostatic strain. The expected slope for a Poisson ratio $\nu = 0.33$ is shown as a black line.

Recording Raman spectra with circular corotating light is ideal for measuring the mean frequencies $\overline{\omega_G}$ and $\overline{\omega_{2D}}$ because the two peak components of the G and 2D mode have the same intensity. For linear light polarization, in contrast, one of the peaks may be absent prohibiting the evaluation of the mean frequencies. While equally intense G^+ and G^- peaks may also be realized with linearly polarized excitation and unpolarized detection [18], this is impossible for the 2D mode because of its peculiar polarization dependence. For example, only the $2D^-$ component was detected in [18] with unpolarized detection, which can

be also seen when calculating the average intensity of the spectra ↕↕ and ↕↔ in figure 2(b).

We demonstrate the benefit of circular polarization for strain analysis with incrementally increasing uniaxial strain in figure 3(a). Both G and 2D modes were fit by two Lorentzian peaks of same spectral width. We thereby obtained the frequencies of all components, i.e. ω_{G^-}, ω_{G^+}, ω_{2D^-} and ω_{2D^+}, which were used to calculate $\overline{\omega_G}$ and $\overline{\omega_{2D}}$. For low strain levels, when no peak splitting was visible, we obtained the mean frequencies from a single Lorentzian fit. This is only possible because the strain-split G and 2D components have equal intensity, i.e. because we use the circular-corotating configuration in Raman scattering.

In figure 3(b), we plot $\overline{\omega_{2D}}$ and $\overline{\omega_G}$ for varying strain in the correlation plot of 2D and G frequency (green dots, sample U1). The data points follow a linear trend. This shows that we systematically varied the strain at constant doping. The same linear trend was observed for two other graphene flakes, where strain was induced along the armchair direction (samples U2 and U3 in figure 3(b); for spectra see supplementary figure S2). From a linear fit, we obtain the slope for hydrostatic or biaxial strain $\Delta\omega_{2D}^h/\Delta\omega_G^h = 2.21 \pm 0.05$. The value is in excellent agreement with theoretical calculations of Mohr *et al* [38] and measured values on graphene blisters reported by Metten *et al* [35] and Lee *et al* [49]. It also agrees with the experimentally determined slope of 2.45 ± 0.37 measured by Zabel *et al* [37] due to its large margin of error.

The peak position for pristine graphene (i.e. no strain and no doping; yellow star in figure 3(b)) was extracted from electrostatic gating measurements by Das *et al* [17] for the case of zero doping as $\omega_G^0 = 1583\ \mathrm{cm}^{-1}$ and $\omega_{2D}^0 = 2678\ \mathrm{cm}^{-1}$. ω_{2D}^0 was recalculated to account for the different excitation wavelength in our experiment using a 2D mode dispersion of $100\ \mathrm{cm}^{-1}\ \mathrm{eV}^{-1}$ [50]. We note that there is still a slight uncertainty on the spectral positions ω_G^0 and ω_{2D}^0 because of a possible native strain in the measurements of [17]. The G mode frequency at zero doping typically scatters by $\pm 1\ \mathrm{cm}^{-1}$ when comparing similar experiments [17, 28, 29], which is small compared to the frequency shifts by strain and doping observed in our experiments. $\omega_G^0, \omega_{2D}^0$ lies outside the measured 2D versus G frequency line in figure 3(b). This is due to *p*-doping of the graphene flakes by the PMMA substrate [51–53]. $\Delta\omega_{2D}/\Delta\omega_G = 0.55$ for *p*-type doping in the absence of strain is shown as a red line in figure 3(b) [30]. We used the expected G frequency shift under *p*-type doping to estimate the doping of the graphene flakes as $\sim 5 \times 10^{12}\ \mathrm{cm}^{-2}$ ([17], see also [30]).

From the frequency shift and splitting of the G line we calculated the hydrostatic and shear strain giving rise to the spectra in figure 3(a). We used a Grueneisen parameter of $\gamma_G = 1.8$ [18, 34, 35, 37] and shear deformation potential of $\beta_G = 0.99$ [18]. The shear strain increases linearly with hydrostatic strain, which is expected for uniaxial stress (figure 3(b) inset). Hydrostatic strain and shear strain under uniaxial tension are connected by the Poisson ratio ν as $\varepsilon_s = [(1+\nu)/(1-\nu)]\varepsilon_h$. The Poisson ratio is $\nu = 0.33$ for the case of ideal stress-strain transfer from the PMMA beam to graphene [18, 48]. The expected slope agrees well with the data points extracted for sample U1 and U2 (see dots and squares in the inset of figure 3(b)). For sample U3, the shear strain at a given hydrostatic strain is larger than expected. In this experiment the PMMA beam was deflected several times before the measurement was taken, which led to a non-ideal load resulting in a different strain configuration. Extracting hydrostatic and shear strain components is useful for determining the strain configuration and testing the stress-strain transfer from a substrate to graphene. For samples U1 and U2 we observed good agreement of the uniaxial strain calculated from the beam deflection and the uniaxial strain calculated from the measured hydrostatic strain (supplementary figure S3).

1.3. Complex nanoscale strain configurations

So far, we presented one application of our methodology for strain evaluation. Using circular light polarization turned out to be useful for unraveling the local strain and doping levels, especially for weak strain when no peak splitting is detectable. As a second example, we analyze complex and unknown strain configurations on the nanoscale. Exfoliated flakes of graphene were suspended on multiple lithographically-fabricated pairs of gold nanodiscs with diameters of ~100 nm, heights of 40–70 nm and gaps of 20–30 nm (figure 4(a)) [54, 55].

After transfer on top of the nanodimers, the substrate adhesion pulled the graphene into the gap between the two gold nanoparticles. This induced strong local strain with completely unknown configurations (see AFM topography, figure 4(b)). The Raman spectrum from the graphene bridging the dimer gap is strongly enhanced by surface-enhanced Raman scattering [54–56]. The plasmon of the gold nanodimer induces strong electromagnetic near fields that increase the local Raman cross section by three to four orders of magnitude [54]. The near field enhancement provides nanoscale spatial resolution; it also fixes the polarization of the field to be parallel to the nanodimer axis.

Figure 4(c) shows two representative Raman spectra with different levels of intrinsic strain. They belong to the same graphene flake but were recorded on different nanodimers. Both G and 2D modes are split into three components of different intensity. The two peaks with the lowest Raman shift arise from the strained graphene in the interparticle gap [54]. The third peak is only slightly shifted from the peak position expected for pristine graphene (grey dashed lines in figure 4(c)). It arises from the unstrained graphene around the nanodimer that contributes to all Raman spectra without plasmonic enhancement. In the following, we focus

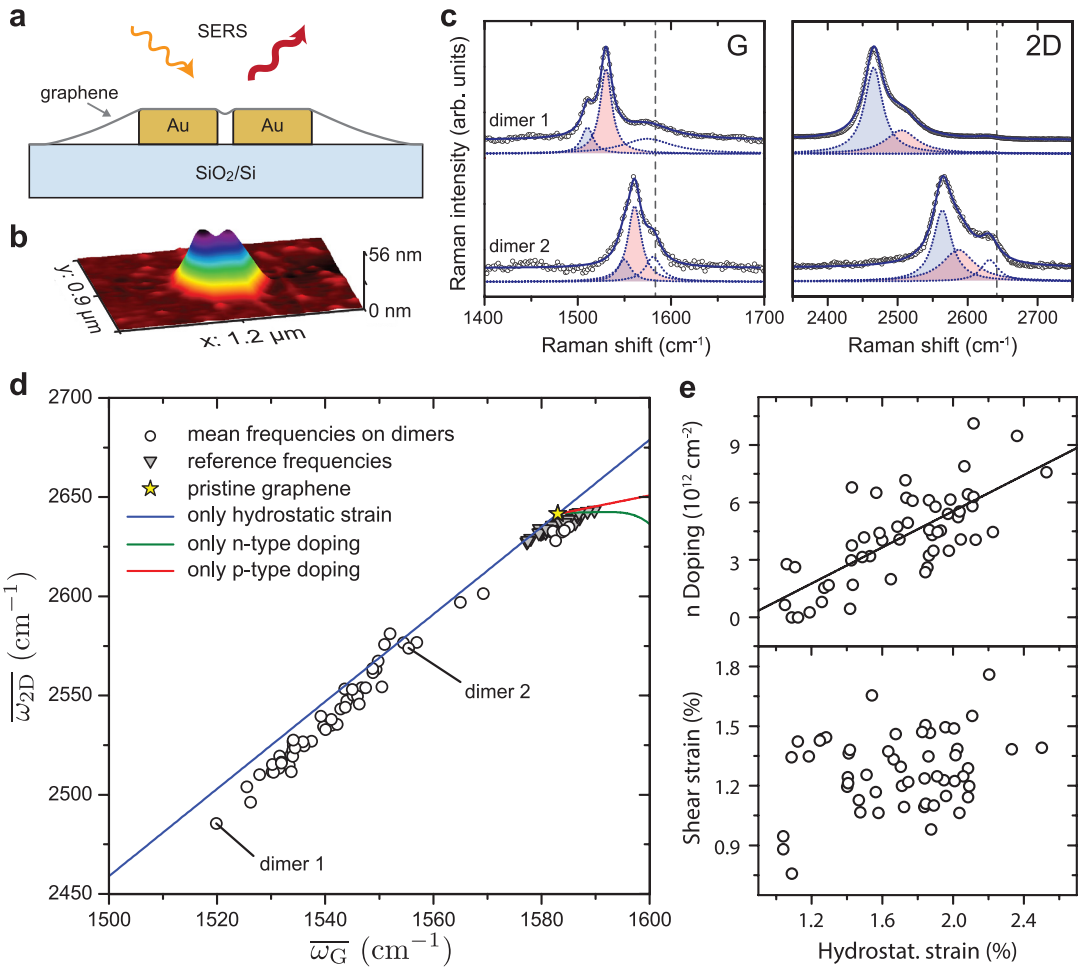

Figure 4. Raman characterization of graphene on gold nanodimers. (a) Geometry of plasmonic nanostructure and substrate. Arrows indicate surface-enhanced Raman scattering (SERS) using graphene as Raman scatterer. (b) Representative 3-dimensional AFM profile of the graphene-covered nanodimer. (c) Exemplary Raman spectra of graphene covering two Au nanodimers with strong (top) and weak (bottom) strain. G^- and $2D^-$ peaks are colored blue, G^+ and $2D^+$ peaks are colored red. The spectral positions for unstrained graphene are indicated by grey dashed lines (sample D1, laser wavelength 638 nm, linear light pol. along dimer axis). (d) Correlation plot of 2D and G mean frequencies (circles). Spectral positions are indicated by triangles for reference measurements on SiO_2/Si. The yellow star shows the frequencies for unstrained and undoped graphene (deduced from experimental data in [29], 633 nm laser excitation, assuming a 2D mode dispersion of 100 cm^{-1} eV^{-1}). Expected peak positions are shown by the blue line for hydrostatic strain (no doping), the red line for *p*-type doping and the green line for *n*-type doping (fit of experimental data in [30], no strain). (e) Extracted magnitudes of doping, shear strain and hydrostatic strain induced in graphene by the nanodimers. A linear fit is superimposed on the data in the upper plot.

on the two peaks that are shifted to lower wavenumbers and thereby analyze the local strain in the dimer cavity. We identify these as the G^- and G^+ or $2D^-$ and $2D^+$ components. The spectra show clear signatures of hydrostatic strain (peak shift) and shear strain (peak splitting).

We now turn to a statistical analysis of the strain and doping locally induced in different positions of a graphene flake by various nanodimers. The dimers were individually addressed with a confocal Raman microscope. We recorded the Raman spectra of 60 graphene-covered gold nanodimers, all of which showed surface-enhanced Raman scattering. We calculated the mean frequencies $\overline{\omega_G}$ and $\overline{\omega_{2D}}$ from fits similar to figure 4(c) for each nanodimer. The contributions of doping and hydrostatic strain were separated with a correlation plot of the mean 2D and G frequencies shown in figure 4(d). The peak positions are strongly shifted compared to the reference measurements 1 μm away from each nanodimer (grey triangles) and of pristine graphene (yellow star). To determine the local hydrostatic strain, we needed to analyse the contribution of local charge doping first. We assumed an *n*-type doping in the graphene bridging the dimer cavity, as previously observed for graphene on gold nanoparticles [57–60]. The ω_{2D}/ω_G positions for *n*-type doping were obtained from a fit of the experimental data in [30] and are plotted as a green line in figure 4(d). The local *n*-type doping was calculated from the expected G frequency shifts [28]. It reached levels of up to 10^{13} cm^{-2}, see figure 4(e). This is more than one order of magnitude higher than the maximum doping levels of 6×10^{11} cm^{-2} for a comparable plasmonic system reported in [60]. This is expected because we probe the local doping in graphene in the vicinity of the gold nanoparticles, whereas Fang *et al* [60] probed the

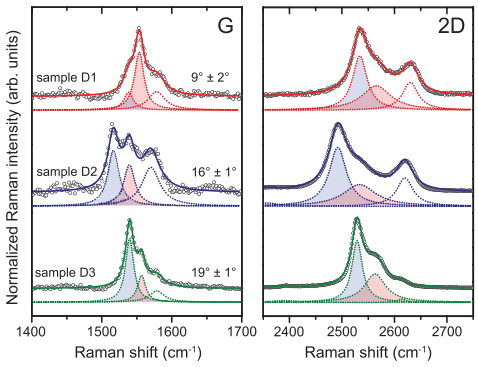

Figure 5. Strain evaluation for several graphene flakes covering gold nanodimers (samples D1–D3, laser wavelength 638 nm, linear light pol. along dimer axes). Exemplary Raman spectra are shown for three samples. Fits with three Lorentzian peaks are superimposed on the experimental data and offset for clarity. G^- and $2D^-$ components are colored blue and G^+ and $2D^+$ components red. The angles between the zigzag direction in the graphene lattice and the dimer axes were calculated from I_{G^-}/I_{G^+} and are given next to the spectra.

charge doping of the entire graphene sheet by transport measurements. Our approach complements the macroscopic measurements with an opportunity to probe local doping levels in an area of $\sim 20 \times 20\,\mathrm{nm}^2$. Interestingly, the local charge doping increased statistically with the hydrostatic strain (figure 4(e), calculated using a Grueneisen parameter of $\gamma_G = 1.8$ [18, 34, 35, 37]). We expect that with increasing local strain, graphene is pulled deeper into the dimer cavity. This leads to a stronger interaction between graphene and the gold nanostructure and explains the increase in doping with strain.

The nanodimers induced strong local strain in the graphene lattice with a hydrostatic component ranging from 1% to 2.5% (figure 4(e)). The shear component was calculated from the G splitting using a shear deformation potential of $\beta_G = 0.99$ [18]. With a magnitude from 0.75% to 1.8% it was weaker than the hydrostatic component (figure 4(e)). This differs from uniaxial strain, where the shear component was twice as large as the hydrostatic component (figure 3(b) inset) and biaxial strain where the shear component vanishes. Shear strain and hydrostatic strain are largely uncorrelated for the nanodimers (figure 4(e)), from which we conclude that the nanodimers induce different strain configurations in the suspended graphene. Our methodology for strain evaluation is even applicable for this complicated case because it does not require any assumption of the strain configuration as an input parameter.

Finally, we demonstrate our analysis of local strain and doping for several different graphene flakes covering arrays of gold nanodimers. Representative Raman spectra of three graphene flakes (samples D1–D3) are shown in figure 5. While the intensity ratio of the $2D^-$ and $2D^+$ components is similar in all spectra, the G^-/G^+-intensity ratio varies from one flake to the other. This is explained by the different lattice orientation of the graphene flakes with respect to the direction of the local shear-strain component (see methods section) [18, 19]. Based on symmetry arguments as discussed in detail in [54] we assume that the local shear strain is directed along and perpendicular to the dimer axis. We determined the angle between the zigzag direction of graphene and the dimer axis for 86 nanodimers covered by five different graphene flakes (supplementary figure S4(a)). The estimated angles range from $(9 \pm 2)^\circ$ for sample D1 to $(19 \pm 1)^\circ$ for D3. We also repeated the correlation analysis of the 2D and G mean frequencies for all graphene flakes (supplementary figure S4(b)). The peak positions nicely follow the same trend as for sample D1 in figure 4(d). We found statistically the same strain and doping levels in all graphene flakes.

Our methodology is generally also applicable to other 2D materials than graphene. It requires two Raman modes ω_{pn1} and ω_{pn2} with a different shift $\Delta\omega^h_{pn1}/\Delta\omega^h_{pn2}$ induced by hydrostatic strain than the shift $\Delta\omega^d_{pn1}/\Delta\omega^d_{pn2}$ induced by doping. $\Delta\omega^d_{pn1}/\Delta\omega^d_{pn2}$ is particularly large for graphene because of the nonadiabatic Kohn anomaly of the G mode [31, 32]. The separation of frequency shifts from strain and doping is, however, still feasible as was shown in recent works for MoS_2 [61, 62].

2. Conclusion

In conclusion, we proposed a method for analyzing arbitrary strain configurations and simultaneous doping in graphene using Raman spectroscopy. First, the shift due to pure hydrostatic strain is determined through explicit or implicit (circular light polarization) averaging of the G and 2D mode components. Second, the peak shifts induced by hydrostatic strain and doping are separated by a correlation analysis of the G and 2D mean frequencies. This offers the possibility to calculate the local shear strain, hydrostatic strain and doping without any assumption on the underlying strain configuration. We performed the suggested strain analysis for graphene in two exemplary situations. Graphene was subjected to uniaxial stress by deflection of a PMMA beam. With this example we showed how circular corotating light naturally yields the mean frequencies of the G and 2D mode under strain. This approach works for low strain levels when no peak splitting is visible. In the second example, graphene was suspended on pairs of gold nanoparticles, which induced strong local strain of unknown configuration. Surface-enhanced Raman scattering allowed extracting the local strain and doping levels with nanoscale resolution. The two examples serve as model cases for the analysis of arbitrary strain in graphene. Our methodology also carries over to other 2D materials, such as MoS_2 [61–63].

3. Methods

3.1. Sample fabrication and characterization

For the measurements under uniaxial strain, monolayer graphene flakes were obtained by micromechanical exfoliation and deposited on a flexible PMMA beam. Prior to graphene transfer, the PMMA substrate was spin coated with SU8 photoresist (SU8 2000.5, MicroChem). The samples were soft-cured at 80 °C for 30 min and exposed to UV radiation (366 nm, 30 s). Graphene was transferred onto the samples with the scotch-tape method. Finally, the samples were covered with PMMA (1% in anisole) to improve the strain transfer efficiency. Uniaxial stress was induced by bending the PMMA beam with a jig (see e.g. [45, 46]). We assume that the doping does not change when inducing strain in graphene by deflection of the PMMA substrate, as we observed no systematic linewidth change of the G peak components with increasing strain. Moreover it was recently shown by Kelvin probe force microscopy measurements that the PMMA substrate most likely acts as a charge reservoir maintaining the doping level constant [64]. To avoid heating and accompanying structural change of the graphene-PMMA interface, we used laser powers below 150 μW for Raman characterization (532 nm laser excitation).

The graphene-covered gold nanodimers were fabricated using the same procedure as described in [54]. In short, gold nanodisk dimers were produced with electron-beam lithography, followed by metallization (5 nm Cr or Ti and 40 to 80 nm Au) and lift-off in an ultrasonic bath. Micromechanically cleaved large flakes of single-layer graphene were then transferred on top of the plasmonic nanostructures using a dry transfer method. The spacing between the nanodimers beneath the graphene flakes was much larger than the laser-spot size. This enabled us to record Raman spectra of graphene interacting with an individual nanodimer.

Raman spectra were recorded with a Horiba XploRA single-grating confocal Raman spectrometer, equipped with a 1200 groves per mm grating, which leads to a spectral resolution of 2–3 cm^{-1}. The spectrometer was calibrated with the Raman response of diamond. 532 nm laser excitation was used for measurements on graphene under uniaxial stress (2 × 120 s acquisition time, 130 μW laser power, spot size of 340 nm). Reference spectra of the PMMA substrate were recorded with the same parameters next to the graphene flakes and subtracted from the Raman spectra of graphene. The graphene-covered gold nanodimers were characterized with 638 nm laser excitation (2 × 120 s acquisition time, 280 μW laser power, spot size of 605 nm); at this wavelength large plasmonic enhancement is expected [54]. The laser was focused on each plasmonic nanodimer using a piezo stage and steps of 100 nm in x-, y- and z direction until a maximum intensity of the 2D mode was achieved. Linear light polarization was chosen along the dimer axis. Reference spectra were recorded 1 μm away from each nanodimer.

3.2. Polarization dependent measurements

The Raman intensities of the G components can be calculated with the macroscopic theory of Raman scattering as $I_{\mathrm{G}\pm} \propto |\mathbf{e}_\mathrm{i} R_{\mathrm{G}\pm} \mathbf{e}_\mathrm{s}|^2$. $\mathbf{e}_\mathrm{i}$ is the polarization of the incoming light and $\mathbf{e}_\mathrm{s}$ of the Raman-scattered light. $R_{\mathrm{G}-}$ is the Raman tensor for the G^- peak and $R_{\mathrm{G}+}$ for the G^+ peak [19]. For uniaxial stress applied at an angle ϑ with respect to the crystallographic zigzag direction in graphene, the intensities are calculated with the Raman tensors given in [19] as

$$\begin{aligned} I_{\mathrm{G}+} &\propto d^2 \cos(\varphi + \psi + 3\vartheta)^2, \\ I_{\mathrm{G}-} &\propto d^2 \sin(\varphi + \psi + 3\vartheta)^2, \end{aligned} \tag{4}$$

where d is the Raman tensor component of the G mode for unstrained graphene. φ is the angle of the incoming light and ψ the angle of the Raman scattered light to the strain axis. From equation (4) it is apparent that $I_{\mathrm{G}-}$ and $I_{\mathrm{G}+}$ can be very different; for $\varphi + \psi + 3\vartheta = n \cdot \pi/2$ (n integer) one of the components vanishes. The situation is different for circular light polarization with polarization vectors [65]

$$\mathbf{e}_{\circlearrowleft} = \frac{1}{\sqrt{2}} \begin{pmatrix} 1 \\ -\mathrm{i} \end{pmatrix}, \quad \mathbf{e}_{\circlearrowright} = \frac{1}{\sqrt{2}} \begin{pmatrix} 1 \\ \mathrm{i} \end{pmatrix}. \tag{5}$$

For circular corotating polarization (i.e. $\circlearrowleft\circlearrowleft$ or $\circlearrowright\circlearrowright$ as combinations for $\mathbf{e}_\mathrm{i}$ and $\mathbf{e}_\mathrm{s}$) we obtain $I_{\mathrm{G}-} \propto d^2$ and $I_{\mathrm{G}+} \propto d^2$; the G mode splits into components of equal intensity. When using circular contrarotating polarization (i.e. $\circlearrowleft\circlearrowright$ or $\circlearrowright\circlearrowleft$), both G mode components vanish.

The polarization dependence of the 2D mode is more complex because it is a second-order Raman process. The intensities of the $\mathrm{2D}^-$ and $\mathrm{2D}^+$ components are determined by double-resonance processes and the simple theoretical treatment that was used for the G mode cannot be applied [33, 42, 44]. If incoming- and outgoing light are linearly polarized along the strain axis ($\updownarrow\updownarrow$), $I_{\mathrm{2D}-} > I_{\mathrm{2D}+}$. The opposite case $I_{\mathrm{2D}-} < I_{\mathrm{2D}+}$ is observed for light polarizations perpendicular to the strain axis ($\leftrightarrow\leftrightarrow$). In general there is a complicated functional dependence of $I_{\mathrm{2D}-}$ and $I_{\mathrm{2D}+}$ on the polarization directions of incoming and outgoing light [33]. A reliable fit of the 2D peak components is only possible for a large peak splitting induced by shear strain. For circular light polarization, the overall peak intensity is determined by the selection rules of the Raman process. The 2D mode has symmetry $A_{1g} \oplus E_{2g}$ [66]. Under circular corotating polarization processes with A_{1g} symmetry vanish whereas for circular contrarotating polarization processes with E_{2g} symmetry are zero [65]. This explains the non-vanishing 2D mode for both, circular corotating and contrarotating light polarization.

For Raman measurements with circular light polarization, we used an optical setup as schematically

depicted in figure 2(a). The laser beam with initially linear light polarization was directed through a quarter-wave plate ($\lambda/4$) to induce circular light polarization. The light was focused onto the sample with an optical microscope which was also used to collect the backscattered light. After the beam splitter (BS) and notch filter (NF), a second quarter-wave plate switched back to linear light polarization. With an analyzer, we selected either the circular-corotating or the circular-contrarotating polarization in the Raman experiment. In front of the spectrometer entrance we placed a half-wave plate ($\lambda/2$) to ensure that the Raman-scattered light entered the spectrometer always with the same light polarization because the spectrometer response depends on polarization. To realize co- and contrarotating configurations, it is also possible to use a single $\lambda/4$ plate between beam splitter and microscope objective if the setup permits [65]. Combinations of linear light polarization were realized by using $\lambda/2$ plates instead of $\lambda/4$ plates.

Acknowledgments

The authors thank V Oddone and E Grelich for help on construction of a jig to induce uniaxial strain in graphene. NSM thanks Deutsche Telekom Stiftung for financial support. OF acknowledges the support of Czech Science Foundation (GACR 17-18702S), MK and MPA the support of MSMT ERC-CZ project (LL 1301). SH and AV acknowledge funding from the Engineering and Physical Sciences Research council grant EP/K016946/1. FS acknowledges funding from the European Graphene Flagship Project and the ERC Synergy grant Hetero2D. CG, KP and JP acknowledge the financial support of the "*Graphene Core 1, GA: 696656–Graphene-based disruptive technologies*", which is implemented under the EU-Horizon 2020 Research & Innovation Actions (RIA) and is financially supported by EC-financed parts of the Graphene Flagship and of the European Research Council (ERC Advanced Grant 2013) via project no. 321124, 'Tailor Graphene'.

ORCID iDs

Niclas S Mueller https://orcid.org/0000-0002-8688-1974
Sebastian Heeg https://orcid.org/0000-0002-6485-3083
Martin Kalbáč https://orcid.org/0000-0001-9574-4368
Stephanie Reich https://orcid.org/0000-0002-2391-0256

References

[1] Geim A K and Novoselov K S 2007 The rise of graphene *Nat. Mater.* **6** 183–91
[2] Novoselov K S, Fal'ko V I, Colombo L, Gellert P R, Schwab M G and Kim K 2012 A roadmap for graphene *Nature* **490** 192–200
[3] Ishigami M, Chen J H, Cullen W G, Fuhrer M S and Williams E D 2007 Atomic structure of graphene on SiO_2 *Nano Lett.* **7** 1643–8
[4] Couto N J G, Costanzo D, Engels S, Ki D-K, Watanabe K, Taniguchi T, Stampfer C, Guinea F and Morpurgo A F 2014 Random strain fluctuations as dominant disorder source for high-quality on-substrate graphene devices *Phys. Rev.* X **4** 041019
[5] Neumann C *et al* 2015 Raman spectroscopy as probe of nanometre-scale strain variations in graphene *Nat. Commun.* **6** 8429
[6] Bao W, Miao F, Chen Z, Zhang H, Jang W, Dames C and Lau C N 2009 Controlled ripple texturing of suspended graphene and ultrathin graphite membranes *Nat. Nanotechnol.* **4** 562–6
[7] Ahn G, Kim H R, Ko T Y, Choi K, Watanabe K, Taniguchi T, Hong B H and Ryu S 2013 Optical probing of the electronic interaction between graphene and hexagonal boron nitride *ACS Nano* **7** 1533–41
[8] Woods C R 2014 Commensurate-incommensurate transition in graphene on hexagonal boron nitride *Nat. Phys.* **10** 451–6
[9] Ryu S, Liu L, Berciaud S, Yu Y-J, Liu H, Kim P, Flynn G W and Brus L E 2010 Atmospheric oxygen binding and hole doping in deformed graphene on a SiO_2 substrate *Nano Lett.* **10** 4944–51
[10] Kim H H, Yang J W, Jo S B, Kang B, Lee S K, Bong H, Lee G, Kim K S and Cho K 2013 Substrate-induced solvent intercalation for stable graphene doping *ACS Nano* **7** 1155–62
[11] Si C, Sun Z and Liu F 2016 Strain engineering of graphene: a review *Nanoscale* **8** 3207–17
[12] Si C, Liu Z, Duan W and Liu F 2013 First-principles calculations on the effect of doping and biaxial tensile strain on electron–phonon coupling in graphene *Phys. Rev. Lett.* **111** 196802
[13] Levy N, Burke S A, Meaker K L, Panlasigui M, Zettl A, Guinea F, Neto A H C and Crommie M F 2010 Strain-induced pseudo-magnetic fields greater than 300 tesla in graphene nanobubbles *Science* **329** 544–7
[14] Guinea F, Katsnelson M I and Geim A K 2010 Energy gaps and a zero-field quantum hall effect in graphene by strain engineering *Nat. Phys.* **6** 30–3
[15] Ferrari A C *et al* 2006 Raman spectrum of graphene and graphene layers *Phys. Rev. Lett.* **97** 187401
[16] Malard L, Pimenta M, Dresselhaus G and Dresselhaus M 2009 Raman spectroscopy in graphene *Phys. Rep.* **473** 51–87
[17] Das A *et al* 2008 Monitoring dopants by Raman scattering in an electrochemically top-gated graphene transistor *Nat. Nanotechnol.* **3** 210–5
[18] Mohiuddin T M G *et al* 2009 Uniaxial strain in graphene by raman spectroscopy: *g* peak splitting, grüneisen parameters and sample orientation *Phys. Rev.* B **79** 205433
[19] Huang M, Yan H, Chen C, Song D, Heinz T F and Hone J 2009 Phonon softening and crystallographic orientation of strained graphene studied by raman spectroscopy *Proc. Natl Acad. Sci. USA* **106** 7304–8
[20] Lee J E, Ahn G, Shim J, Lee Y S and Ryu S 2012 Optical separation of mechanical strain from charge doping in graphene *Nat. Commun.* **3** 1024
[21] Lee D, Ahn G and Ryu S 2014 Two-dimensional water diffusion at a graphene–silica interface *J. Am. Chem. Soc.* **136** 6634–42
[22] Frank O, Vejpravova J, Holy V, Kavan L and Kalbac M 2014 Interaction between graphene and copper substrate: the role of lattice orientation *Carbon* **68** 440–51
[23] Drögeler M, Volmer F, Wolter M, Terrés B, Watanabe K, Taniguchi T, Güntherodt G, Stampfer C and Beschoten B 2014 Nanosecond spin lifetimes in single- and few-layer graphene-hbn heterostructures at room temperature *Nano Lett.* **14** 6050–5
[24] McCreary K M, Hanbicki A T, Robinson J T, Cobas E, Culbertson J C, Friedman A L, Jernigan G G and Jonker B T 2014 Large-area synthesis of continuous and uniform MoS_2 monolayer films on graphene *Adv. Funct. Mater.* **24** 6449–54
[25] Anagnostopoulos G, Androulidakis C, Koukaras E N, Tsoukleri G, Polyzos I, Parthenios J, Papagelis K and Galiotis C 2015 Stress transfer mechanisms at the submicron level

for graphene/polymer systems *ACS Appl. Mater. Interfaces* **7** 4216–23
[26] Bronsgeest M S, Bendiab N, Mathur S, Kimouche A, Johnson H T, Coraux J and Pochet P 2015 Strain relaxation in cvd graphene: Wrinkling with shear lag *Nano Lett.* **15** 5098–104
[27] Godel F, Mouafo L D N, Froehlicher G, Doudin B, Berciaud S, Henry Y, Dayen J-F and Halley D 2017 Conductance oscillations in a graphene/nanocluster hybrid material: toward large-area single-electron devices *Adv. Mater.* **29** 1604837
[28] Das A, Chakraborty B, Piscanec S, Pisana S, Sood A K and Ferrari A C 2009 Phonon renormalization in doped bilayer graphene *Phys. Rev.* B **79** 155417
[29] Bruna M, Ott A K, Ijäs M, Yoon D, Sassi U and Ferrari A C 2014 Doping dependence of the raman spectrum of defected graphene *ACS Nano* **8** 7432–41
[30] Froehlicher G and Berciaud S 2015 Raman spectroscopy of electrochemically gated graphene transistors: geometrical capacitance, electron–phonon, electron–electron and electron-defect scattering *Phys. Rev.* B **91** 205413
[31] Lazzeri M and Mauri F 2006 Nonadiabatic kohn anomaly in a doped graphene monolayer *Phys. Rev. Lett.* **97** 266407
[32] Pisana S, Lazzeri M, Casiraghi C, Novoselov K S, Geim A K, Ferrari A C and Mauri F 2007 Breakdown of the adiabatic Born–Oppenheimer approximation in graphene *Nat. Mater.* **6** 198–201
[33] Yoon D, Son Y-W and Cheong H 2011 Strain-dependent splitting of the double-resonance raman scattering band in graphene *Phys. Rev. Lett.* **106** 155502
[34] Ding F, Ji H, Chen Y, Herklotz A, Dörr K, Mei Y, Rastelli A and Schmidt O G 2010 Stretchable graphene: a close look at fundamental parameters through biaxial straining *Nano Lett.* **10** 3453–8
[35] Metten D, Federspiel F M C, Romeo M and Berciaud S 2014 All-optical blister test of suspended graphene using micro-raman spectroscopy *Phys. Rev. Appl.* **2** 054008
[36] Metzger C, Rémi S, Liu M, Kusminskiy S V, Castro Neto A H, Swan A K and Goldberg B B 2010 Biaxial strain in graphene adhered to shallow depressions *Nano Lett.* **10** 6–10
[37] Zabel J, Nair R R, Ott A, Georgiou T, Geim A K, Novoselov K S and Casiraghi C 2012 Raman spectroscopy of graphene and bilayer under biaxial strain: bubbles and balloons *Nano Lett.* **12** 617–21
[38] Mohr M, Maultzsch J and Thomsen C 2010 Splitting of the raman 2*d* band of graphene subjected to strain *Phys. Rev.* B **82** 201409
[39] Ganesan S, Maradudin A and Oitmaa J 1970 A lattice theory of morphic effects in crystals of the diamond structure *Ann. Phys.* **56** 556–94
[40] Reich S, Jantoljak H and Thomsen C 2000 Shear strain in carbon nanotubes under hydrostatic pressure *Phys. Rev.* B **61** R13389–92
[41] Thomsen C, Reich S and Ordejon P 2002 *Ab initio* determination of the phonon deformation potentials of graphene *Phys. Rev.* B **65** 7
[42] Huang M, Yan H, Heinz T F and Hone J 2010 Probing strain-induced electronic structure change in graphene by raman spectroscopy *Nano Lett.* **10** 4074–9
[43] Frank O *et al* 2011 Raman 2d-band splitting in graphene: theory and experiment *ACS Nano* **5** 2231–9
[44] Narula R, Bonini N, Marzari N and Reich S 2012 Dominant phonon wave vectors and strain-induced splitting of the 2*d* raman mode of graphene *Phys. Rev.* B **85** 115451
[45] Tsoukleri G, Parthenios J, Papagelis K, Jalil R, Ferrari A C, Geim A K, Novoselov K S and Galiotis C 2009 Subjecting a graphene monolayer to tension and compression *Small* **5** 2397–402
[46] Frank O, Tsoukleri G, Parthenios J, Papagelis K, Riaz I, Jalil R, Novoselov K S and Galiotis C 2010 Compression behavior of single-layer graphenes *ACS Nano* **4** 3131–8
[47] Galiotis C, Frank O, Koukaras E N and Sfyris D 2015 Graphene mechanics: current status and perspectives *Annu. Rev. Chem. Biomol. Eng.* **6** 121–40
[48] del Corro E, Kavan L, Kalbac M and Frank O 2015 Strain assessment in graphene through the raman 2d mode *J. Phys. Chem.* C **119** 25651–6
[49] Lee J-U, Yoon D and Cheong H 2012 Estimation of youngs modulus of graphene by raman spectroscopy *Nano Lett.* **12** 4444–8
[50] Thomsen C and Reich S 2000 Double resonant raman scattering in graphite *Phys. Rev. Lett.* **85** 5214–7
[51] Pirkle A *et al* 2011 The effect of chemical residues on the physical and electrical properties of chemical vapor deposited graphene transferred to sio2 *Appl. Phys. Lett.* **99** 122108
[52] Gammelgaard L, Caridad J M, Cagliani A, Mackenzie D M A, Petersen D H, Booth T J and Bøggild P 2014 Graphene transport properties upon exposure to pmma processing and heat treatments *2D Mater.* **1** 035005
[53] Suk J W, Lee W H, Lee J, Chou H, Piner R D, Hao Y, Akinwande D and Ruoff R S 2013 Enhancement of the electrical properties of graphene grown by chemical vapor deposition via controlling the effects of polymer residue *Nano Lett.* **13** 1462–7
[54] Heeg S, Fernandez-Garcia R, Oikonomou A, Schedin F, Narula R, Maier S A, Vijayaraghavan A and Reich S 2013 Polarized plasmonic enhancement by au nanostructures probed through raman scattering of suspended graphene *Nano Lett.* **13** 301–8
[55] Heeg S, Oikonomou A, Garcia R F, Maier S A, Vijayaraghavan A and Reich S 2013 Strained graphene as a local probe for plasmon-enhanced raman scattering by gold nanostructures *Phys. Status Solidi* RRL **7** 1067–70
[56] Heeg S, Oikonomou A, Fernandez-Garcia R, Lehmann C, Maier S A, Vijayaraghavan A and Reich S 2014 Plasmon-enhanced raman scattering by carbon nanotubes optically coupled with near-field cavities *Nano Lett.* **14** 1762–8
[57] Wu Y *et al* 2012 Tuning the doping type and level of graphene with different gold configurations *Small* **8** 3129–36
[58] Huh S, Park J, Kim K S, Hong B H and Kim S B 2011 Selective *n*-type doping of graphene by photo-patterned gold nanoparticles *ACS Nano* **5** 3639–44
[59] Sławińska J, Wlasny I, Dabrowski P, Klusek Z and Zasada I 2012 Doping domains in graphene on gold substrates: first-principles and scanning tunneling spectroscopy studies *Phys. Rev.* B **85** 235430
[60] Fang Z, Wang Y, Liu Z, Schlather A, Ajayan P M, Koppens F H L, Nordlander P and Halas N J 2012 Plasmon-induced doping of graphene *ACS Nano* **6** 10222–8
[61] Liu X, Balla I, Bergeron H, Campbell G P, Bedzyk M J and Hersam M C 2016 Rotationally commensurate growth of MoS_2 on epitaxial graphene *ACS Nano* **10** 1067–75
[62] Michail A, Delikoukos N, Parthenios J, Galiotis C and Papagelis K 2016 Optical detection of strain and doping inhomogeneities in single layer mos2 *App. Phys. Lett.* **108** 173102
[63] Sun Y, Liu K, Hong X, Chen M, Kim J, Shi S, Wu J, Zettl A and Wang F 2014 Probing local strain at Mx_2-metal boundaries with surface plasmon-enhanced raman scattering *Nano Lett.* **14** 5329–34
[64] Chhikara M, Gaponenko I, Paruch P and Kuzmenko A B 2017 Effect of uniaxial strain on the optical drude scattering in graphene *2D Mater.* **4** 025081
[65] Reich S, Thomsen C, Duesberg G S and Roth S 2001 Intensities of the raman-active modes in single and multiwall nanotubes *Phys. Rev.* B **63** 041401
[66] Jorio A, Mueller N S and Reich S 2017 Symmetry-derived selection rules for plasmon-enhanced raman scattering *Phys. Rev.* B **95** 155409